

## Interseismic Strain Localization in the San Jacinto Fault Zone

ERIC O. LINDSEY,<sup>1</sup> VALERIE J. SAHAKIAN,<sup>1</sup> YURI FIALKO,<sup>1</sup> YEHUDA BOCK,<sup>1</sup> SYLVAIN BARBOT,<sup>2</sup> and THOMAS K. ROCKWELL<sup>3</sup>

**Abstract**—We investigate interseismic deformation across the San Jacinto fault at Anza, California where previous geodetic observations have indicated an anomalously high shear strain rate. We present an updated set of secular velocities from GPS and InSAR observations that reveal a 2–3 km wide shear zone deforming at a rate that exceeds the background strain rate by more than a factor of two. GPS occupations of an alignment array installed in 1990 across the fault trace at Anza allow us to rule out shallow creep as a possible contributor to the observed strain rate. Using a dislocation model in a heterogeneous elastic half space, we show that a reduction in shear modulus within the fault zone by a factor of 1.2–1.6 as imaged tomographically by ALLAM and BEN-ZION (Geophys J Int 190:1181–1196, 2012) can explain about 50 % of the observed anomalous strain rate. However, the best-fitting locking depth in this case ( $10.4 \pm 1.3$  km) is significantly less than the local depth extent of seismicity (14–18 km). We show that a deep fault zone with a shear modulus reduction of at least a factor of 2.4 would be required to explain fully the geodetic strain rate, assuming the locking depth is 15 km. Two alternative possibilities include fault creep at a substantial fraction of the long-term slip rate within the region of deep microseismicity, or a reduced yield strength within the upper fault zone leading to distributed plastic failure during the interseismic period.

**Key words:** Fault zone, dislocation model, compliant zone, San Jacinto fault, Anza.

### 1. Introduction

The San Jacinto fault is historically the most seismically active fault in southern California, with

nine major (M 6–7) earthquakes over the past 120 years. The fault segment near Anza has not ruptured for more than 200 years (ROCKWELL *et al.* 2006), and is considered to represent a “seismic gap” (THATCHER *et al.* 1975; SANDERS and KANAMORI 1984). As a result, the Anza segment of the San Jacinto fault (SJF) has been a subject of numerous geologic, geodetic, and seismic studies (ROCKWELL *et al.* 1990; LISOWSKI *et al.* 1991; ALLAM and BEN-ZION 2012).

Early trilateration surveys and electronic distance measurements (EDM) suggested an unusually high strain rate across this segment (LISOWSKI *et al.* 1991; JOHNSON *et al.* 1994). These observations were interpreted as requiring a locking depth of just 5–6 km assuming a homogeneous elastic model, significantly shallower than the observed 14–18 km depth extent of microseismicity in the area (e.g., SANDERS 1990; LIN *et al.* 2007; HAUSSON *et al.* 2012). LISOWSKI *et al.* (1991) proposed that the apparent disagreement could be explained by a compliant fault zone with significantly reduced shear modulus, but could not rule out alternatives such as shallow fault creep, which might affect near-field measurements. More recently, WADOWSKI (2009) proposed that the deep microseismicity may be due to the propagation of “brittle creep” into the seismogenic zone, and, therefore, the locking depth is in fact much shallower than the bottom of the seismogenic zone.

Shallow creep on the Anza segment of the SJF would offset geodetic monuments on either side of the fault and increase the apparent near-fault strain rate. Shallow creep is predicted by laboratory observations, which show that poorly consolidated rocks in the top few kilometers of the Earth’s crust exhibit velocity-strengthening behavior (MARONE and SCHOLZ 1988; MARONE 1998), and by rate- and state-dependent frictional models in which low normal stresses

---

**Electronic supplementary material** The online version of this article (doi:10.1007/s00024-013-0753-z) contains supplementary material, which is available to authorized users.

---

<sup>1</sup> Institute of Geophysics and Planetary Physics, Scripps Institution of Oceanography, University of California San Diego, La Jolla, CA 92093, USA. E-mail: elindsey@ucsd.edu

<sup>2</sup> Earth Observatory of Singapore, Nanyang Technological University, Singapore 639798, Singapore.

<sup>3</sup> Department of Geological Sciences, San Diego State University, San Diego, CA 92182, USA.

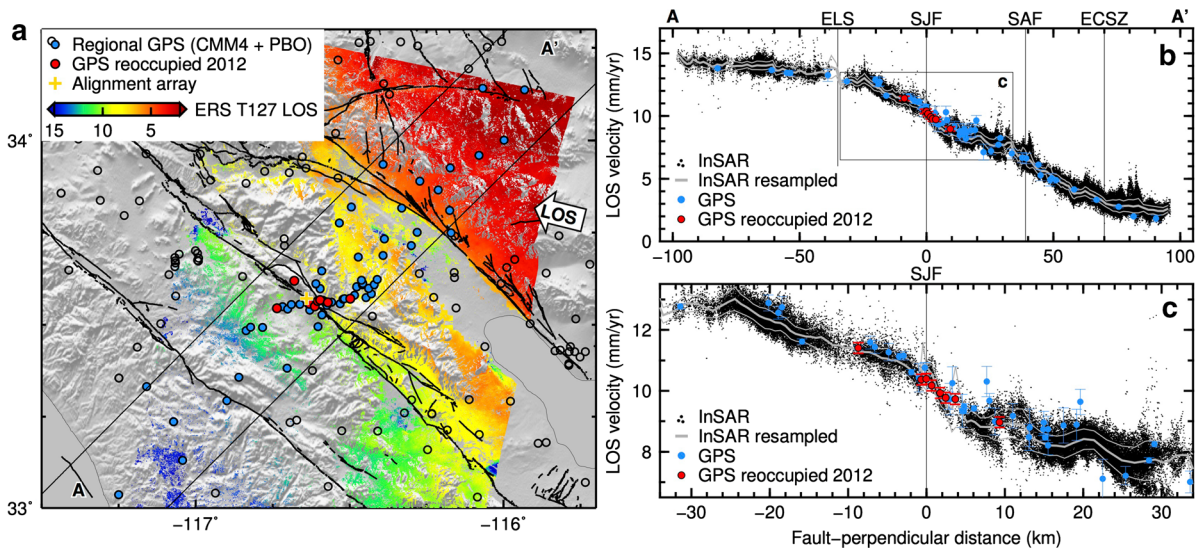


Figure 1

Geodetic data used in this study. **a** Map showing InSAR line-of-sight (LOS) velocities from ERS track 127 (MANZO *et al.* 2011), locations of regional GPS sites, and the re-surveyed Mitchell road alignment array. **b** Selected InSAR LOS velocities and GPS velocities projected onto the radar LOS for comparison. **c** Zoom of (b) near the San Jacinto fault (SJF)

near the surface result in stable sliding, even if the frictional properties are velocity-weakening (e.g., TSE and RICE 1986; LAPUSTA *et al.* 2000; KANEKO *et al.* 2013).

A compliant fault zone with a reduced effective shear modulus would have a similar effect on the surface strain rate even if the fault is locked near the surface. Zones of this type have been inferred in several locations, both geodetically (RYBICKI and KASAHARA 1977; FIALKO *et al.* 2002; CHEN and FREY-MUELLER 2002; FIALKO 2004; HAMIEN and FIALKO 2007; BARBOT *et al.* 2009; JOLIVET *et al.* 2009; CAKIR *et al.* 2012) and seismically (SPUDICH and OLSEN 2001; BEN-ZION *et al.* 2003; COCHRAN *et al.* 2009). Observations of trapped waves along the SJF near Anza have suggested such a zone may be present there as well, with inferred reductions in S-wave velocity of up to 50 % (LI and VERNON 2001; LEWIS *et al.* 2005). Recently, ALLAM and BEN-ZION (2012) conducted a high-resolution tomographic study of the velocity structure surrounding the SJF, yielding clear evidence for a low velocity fault zone extending to a depth of several kilometers.

In this study, we present new high-density GPS and InSAR observations (Fig. 1) and numerical models incorporating recent tomographic results (ALLAM and BEN-ZION 2012) to evaluate the

mechanisms responsible for the anomalous interseismic strain rate at Anza. We find that shallow creep is negligible at this location, based on occupations with GPS of an alignment array installed in 1990 (ROCKWELL *et al.* 1992). Next, we show that a compliant fault zone with properties inferred by ALLAM and BEN-ZION (2012) does play a significant role in the localization of strain, affecting inferences of slip rate, locking depth and ultimately seismic hazard. However, the observed elastic heterogeneity is insufficient to fully reconcile the “geodetic” and “seismic” locking depths on the Anza section of the SJF. Instead, we find that the data require either the deep seismogenic zone to be sliding stably at a significant fraction of the long-term rate, or the shallow fault zone to be deforming inelastically, possibly due to a lower yield strength compared to the ambient crust.

## 2. Alignment Array and Shallow Creep

Shallow creep has been observed on a number of faults in Southern California, including the Coachella segment of the SAF (SIEH and WILLIAMS 1990; RYMER 2000; RYMER *et al.* 2002; LYONS and SANDWELL 2003), the Imperial fault (GOULTY *et al.* 1978; LYONS *et al.*

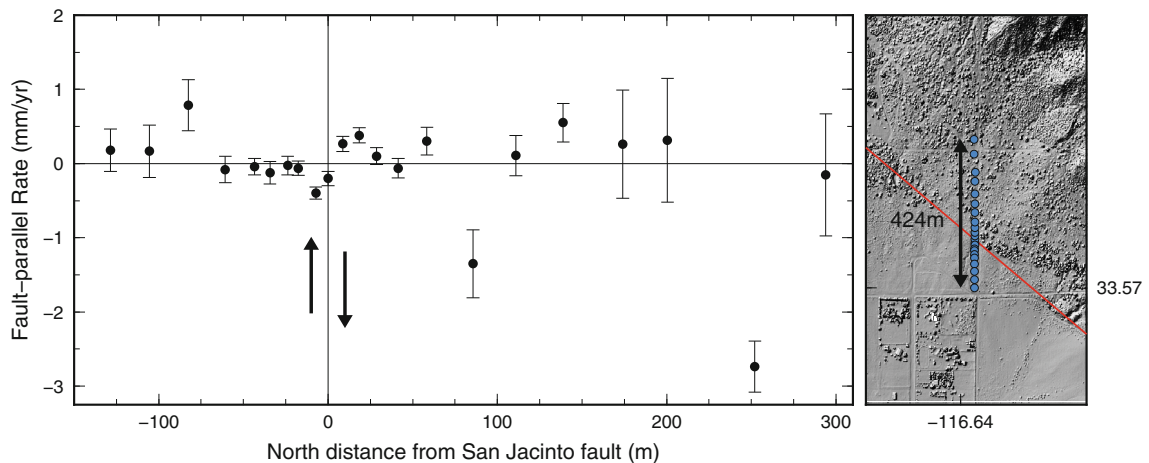


Figure 2

Mitchell road alignment array. Fault-parallel rates computed as total offset divided by the total time, detrended. Arrows indicate expected sense of motion on the fault if creep is occurring. Error bars reflect the sum in quadrature of GPS and Total Station measurement uncertainties. Map shows monument locations relative to the fault trace in red

2002), and the Superstition Hills and Coyote Creek segments of the SJF to the south (SHARP *et al.* 1986; WEI *et al.* 2009, 2011). If shallow creep of this type is occurring on the SJF at Anza, it would offset nearby geodetic monuments and affect the apparent near-field deviatoric strain rate. Here we take advantage of a  $\sim 400$  m-long alignment array installed in 1990 across the SJF at Anza to quantify the near-field interseismic deformation. The Mitchell road array consists of 22 monuments in a line oriented north-south and centered on the fault trace at  $-116.64^{\circ}\text{W}$ ,  $33.572^{\circ}\text{N}$  (Fig. 2). Initial surveys in 1990 and 1991 recorded the azimuth and distance from each monument to the central base station (ROCKWELL *et al.* 1992). In August 2010 and March 2011 we occupied the array with survey-mode GPS. By computing the relative changes in the position of each site, we are able to evaluate the presence of shallow creep at a sub-millimeter per year level.

During each GPS campaign, the monuments were occupied with a tripod-mounted chokering antenna and dual-frequency receiver recording at one sample per second for two separate 15 min intervals; the base station on the fault trace was occupied continuously for the duration of the 2-day campaign. We then computed the instantaneous positions at each epoch relative to the nearby continuous station AZRY, using the Real Time Dynamics software package. This rapid-static approach is justified by error

analyses of the instantaneous positioning method for very small baselines (BOCK *et al.* 2000); in this case we were able to determine the baselines between each site with a one-sigma uncertainty of 2–3 mm in the horizontal direction.

The initial optical surveys determined the azimuth from the base station to each monument at a precision of  $10^{-4}$  degrees, translating to an uncertainty in relative position of 1–15 mm with increasing distance from the base station. In principle, the relative station motions computed over the 20-year period could be used to determine the overall shear strain rate near the fault in addition to any localized creep. However, the expected rotation of the array due to tectonic strain accumulation is on the order of  $10^{-5}$  degrees over the 20-year period, while the initial alignment of the array was subject to a much larger compass error of up to  $1^{\circ}$ . Thus, we subtracted the best-fitting rotation from the differential motion of the benchmarks and focus on near-surface fault creep only. Future GPS surveys of the array should make possible an absolute determination of the local shear strain rate.

In Fig. 2, we show the de-trended offsets in the fault-parallel direction, divided by the total time between observations. The reported uncertainties for each site are the sum in quadrature of the GPS and optical survey errors. These uncertainties are somewhat smaller than overall data scatter, suggesting some non-tectonic motion of individual sites,

possibly related to initial settling and subsequent minor disturbance of the monuments. Nevertheless, no systematic right-lateral offset is visible across the fault trace or anywhere within the array. Formally, comparison of the data with a model of surface creep weighted by the relative measurement uncertainties implies a creep rate of  $<0.2$  mm/year with 95 % confidence.

The evident lack of creep on this segment of the SJF is unsurprising; earlier surveys of another alignment array a few kilometers to the north of the Mitchell road array showed no evidence for surface creep over a period of 7 years between 1977 and 1984 at a level of 1 mm/year (LOUIE *et al.* 1985), although the results were ambiguous owing to motions attributed to the initial settling of the monuments (KELLER *et al.* 1978; SANDERS and KANAMORI 1984). Our measurements confirm the absence of shallow creep on the Anza section of the San Jacinto fault at a significantly increased precision. In contrast, models of rate- and state-dependent friction on faults predict ubiquitous creep within a shallow layer at a rate that is on the order of  $\sim 10$  % of the fault slip rate if the top 2–3 km of the fault are velocity strengthening (e.g., TSE and RICE 1986; LAPUSTA *et al.* 2000). Given the long-term slip rate of the SJF at Anza of 10–15 mm/year (ROCKWELL *et al.* 1990; BLISNIUK *et al.* 2010, also see below) the predicted rate of shallow creep exceeds the observational constraints by nearly an order of magnitude. Possible explanations for this discrepancy include velocity-weakening behavior of the uppermost seismogenic layer (e.g., KANEKO *et al.* 2013), or distributed yielding (see “Discussion”).

### 3. Elastic Half-Space Models

The analysis of geodetically determined interseismic motion near an active fault requires a model, including an assumption about the rheology of Earth’s lithosphere. The most common models are a dislocation in an elastic half-space (SAVAGE and BURFORD 1973), or an elastic layer over a viscoelastic half-space (NUR and MAVKO 1974; SAVAGE and PRESCOTT 1978). In the context of infinitely long strike-slip faults, it was shown that the two models can explain

interseismic deformation equally well (SAVAGE 1990; FAY and HUMPHREYS 2005). Recent simulations that take into account laboratory-constrained rheologies and long-term strain evolution (TAKEUCHI and FIALKO 2012) show a considerable strain localization in the ductile substrate, at least for mature faults such as those of the SAF-SJF system. Thus, in the following, we choose to interpret the data with an elastic dislocation model, in which the fault is fully locked above the locking depth  $D$ , and slipping at the full long-term rate below. Simple dislocation models have shown remarkable success at predicting fault slip rates and locking depths, without significant bias relative to seismic and geologic observations (e.g., SMITH-KONTER *et al.* 2011; LINDSEY and FIALKO 2013). The stress singularity arising from the sudden transition from locked to creeping at the locking depth is non-physical; in reality, the slip rate must increase gradually with depth to the full rate (e.g., SAVAGE 2006). The implications of a more gradual variation in slip rate with depth are considered in Sect. 4.

#### 3.1. Regional GPS Data

The primary dataset used to infer slip rates on the SAF-SJF system consists of GPS velocities from the Southern California Earthquake Center (SCEC) Crustal Motion Map version 4 (CMM4) GPS velocity solution (SHEN *et al.* 2011). We use a combination of the CMM4 dataset and continuous GPS velocities from the UNAVCO Plate Boundary Observatory (PBO) network, rotated into the North America Fixed (NAFD) reference frame (Tom Herring, pers. commun., 2011). This is the same GPS dataset used for determination of fault slip rates in the Uniform California Earthquake Rupture Forecast, Version 3 (UCERF3) project, and contains 2,663 GPS velocities distributed throughout California and other parts of North America. We selected 70 sites located along a 30 km-wide fault-perpendicular profile centered on the SJF at Anza (116.6321W, 33.5679N) and projected the horizontal velocities onto the fault azimuth of  $313^\circ$ . This azimuth was chosen to minimize the trend in the residual fault-perpendicular velocities, which would represent unmodeled fault-normal compression; we note that the results are not sensitive to small changes in this value.

Table 1

*Updated GPS velocities and one-sigma uncertainties for sites reoccupied in September 2012 and April 2013, in mm/year*

Site	Longitude	Latitude	$V_E$	$V_N$	$V_U$	$\sigma_E$	$\sigma_N$	$\sigma_U$
CARY	243.2645	33.5454	-33.43	13.94	-0.45	0.22	0.18	1.00
ANZC	243.3694	33.5578	-31.23	11.93	-0.24	0.21	0.22	1.05
G114	243.3871	33.5502	-31.65	11.57	1.44	0.33	0.23	1.07
TOME	243.3200	33.6190	-30.99	11.36	1.09	0.22	0.21	1.08
G120	243.3970	33.5646	-30.61	10.77	-0.52	0.48	0.42	1.99
RCUT	243.4044	33.5675	-30.14	10.58	0.31	0.29	0.19	1.05
0821	243.4294	33.5613	-30.33	10.21	-0.54	0.19	0.20	1.03
D138	243.5019	33.5711	-28.46	9.03	-0.03	0.31	0.22	1.24

Reference frame is ITRF2008

The dataset, shown in Fig. 1a, has a very dense spacing of GPS sites in the vicinity of Anza: along the entire SJF there are 55 sites located within 10 km of the fault trace, and 26 of these are within our selected profile at Anza. However, many of these are campaign sites with velocities of relatively low accuracy, occupied four to 12 times over the period 1992–2002 when the GPS constellation, orbits, and receivers, especially in the earlier epochs, were less favorable. There were no reported observations in the past 10 years. As a result, the projected velocities show considerable scatter (Fig. 1b). To improve the accuracy of the near-field GPS velocities, in September 2012 and April 2013 we re-occupied eight of the sites near Anza, highlighted in red in Fig. 1. The sites were occupied for 2–4 days at 30-s sampling, and the data were processed in combination with the CMM4 results using the GAMIT/GLOBK software package (HERRING *et al.* 2010). The long timespan between surveys allowed us to determine each velocity with a  $1\sigma$  uncertainty of 0.2–0.5 mm/year.

Although the intervening time period spans several regional earthquakes (notably, the 1994 M6.7 Northridge, 1999 M7.1 Hector Mine, and 2010 M7.2 El Mayor-Cucapah events), the relatively small size of the network compared with the distance to the events means that coseismic and postseismic offsets do not vary significantly between sites, so they should not significantly affect the relative velocities. This is supported by comparison of continuous GPS time-series within the affected region. To further mitigate the effect of these earthquakes, we subtracted the estimated coseismic offsets for each event based on a dislocation model during the GLOBK analysis. The

results are summarized in Table 1 in the ITRF2008 reference frame.

The updated fault-parallel velocities are compared with the regional GPS data in Fig. 1b and c; the best-fitting fault-parallel shear strain rate is  $0.60 \pm 0.10$   $\mu\text{rad}/\text{year}$  for the five sites within 3 km of the fault trace [ $1 \mu\text{rad}/\text{year} = 1$  (mm/year)/km]. Considering the full 18 km span from CARY to D138, the strain rate is  $0.40 \pm 0.05$   $\mu\text{rad}/\text{year}$ , in good agreement with USGS two-color EDM results which covered a similar span across the fault and recorded a rate of  $0.42 \pm 0.05$   $\mu\text{rad}/\text{year}$  (<http://earthquake.usgs.gov/monitoring/edm/socal/>).

### 3.2. InSAR Data

We also incorporate InSAR data from ERS-1/2 descending track 127, processed with the small baseline subset (SBAS) method in combination with a sparse set of five continuous GPS velocities to constrain the longest-wavelength deformation signals and remove orbital and other systematic errors (MANZO *et al.* 2011). The resulting map of surface deformation may retain unmodeled vertical motion or residual errors at long wavelengths, which can lead to biases in slip rate inversions (e.g., FIALKO 2006; LUNDGREN *et al.* 2009; LINDSEY and FIALKO 2013). Therefore, we adopted the remove–restore method proposed by WEI *et al.* (2010) to constrain the long wavelengths using additional continuous GPS data. Using all available continuous GPS data in the area within and surrounding the radar scene, we interpolated the GPS velocities onto each radar pixel using natural neighbor interpolation, then projected these

velocities into the radar LOS. The resulting smooth velocity map was subtracted from the InSAR, and the result was high-pass filtered with a 40 km cutoff wavelength. The interpolated GPS velocities were then added back, resulting in a velocity field that agrees with the GPS at large spatial wavelengths but retains the short-wavelength information provided by the InSAR. Sensitivity testing indicated that the results are not strongly dependent on the interpolation method or the filter cutoff wavelength; for details see WEI *et al.* (2010) or TONG *et al.* (2013).

The final InSAR-derived velocity map is shown in Fig. 1. The western portion of the scene is heavily forested, resulting in poor C-band radar correlation. As a result, there are far fewer available data points there than in the eastern portion of the scene where C-band correlation is excellent. Thus, some resampling of the data is needed to avoid over-fitting the eastern part of the selected profile at the expense of points to the west. We considered uniform resampling, or resampling at a rate proportional to a measure of the model sensitivity (normalized derivative of the model predictions with respect to each of the parameters), but found that a strain-based resampling provided the most faithful reproduction of the original dataset and the smallest resulting parameter uncertainties for a given number of resampled data points. We used LOESS local regression (CLEVELAND 1979; CLEVELAND and DEVLIN 1988) to fit a smooth curve to the data, then divided the profile into bins with a width proportional to the derivative of the smooth curve. The mean and standard deviation of the LOS velocities were computed within each bin; we ultimately recovered 190 velocity estimates with standard deviations ranging from 0.2 to 0.9 mm/year, with the highest sample rate in regions of high strain (see Supplementary Figure S1).

The resampled InSAR profile across the fault is shown in Fig. 1b and c along with LOS-projected horizontal GPS velocities. In the figures, the velocities are referenced to a constant incidence angle of  $23.5^\circ$  for plotting purposes; we used the exact incidence angle for each pixel when comparing the data to a model. The data suggest the region of high strain across the fault is approximately 3 km wide and offset to the east of the surface trace of the fault, with a best-fitting strain rate of  $0.79 \mu\text{rad}/\text{year}$ , slightly higher than the rate determined above from only GPS.

### 3.3. Heterogeneous Material Properties

High resolution double-difference tomography by ALLAM and BEN-ZION (2012) indicates the presence of a significant low velocity anomaly along the SJF near Anza. The result is consistent with earlier observations of fault-zone-trapped waves in the area (LI and VERNON 2001; LEWIS *et al.* 2005), and suggests the presence of an extensive compliant fault zone with a reduced elastic shear modulus, extending several kilometers deep and up to several kilometers from the fault.

We used the seismic velocity model of ALLAM and BEN-ZION (2012) to compute the shear modulus along a 2D fault-perpendicular transect at the location of the geodetic profile, using an empirical relation to compute density from  $V_p$  (LUDWIG *et al.* 1970; BROCHER 2005). The result is shown in Fig. 3a. We then computed the elastic Green functions for anti-plane dislocations representing each fault at a range of locking depths, using the method of fictitious body forces (BARBOT *et al.* 2009) implemented in a parallel finite-difference framework. As an example, the surface velocity due to a dislocation at 10 km depth is compared for the homogeneous and heterogeneous models in Fig. 3b. The strain rate near the fault is increased by up to 50 %, and the velocities are

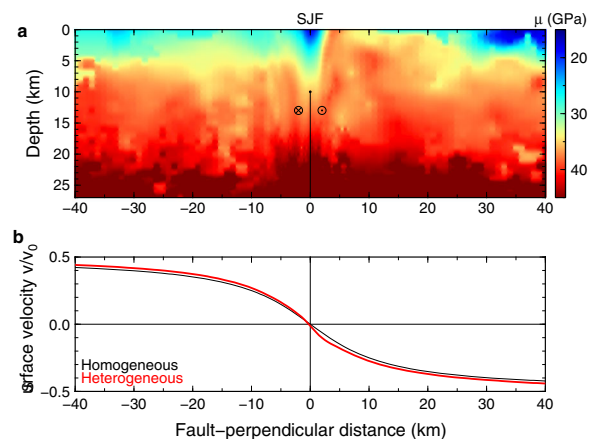


Figure 3

**a** Fault-perpendicular cross-section showing shear modulus values inferred from tomography of ALLAM and BEN-ZION (2012), centered on the fault trace at Anza (116.632W, 33.568N). **b** Predicted fault-parallel surface velocity for a unit dislocation slipping freely below 10 km, in a homogeneous (black) and heterogeneous (red) elastic domain

somewhat asymmetric across the fault trace, in qualitative agreement with the geodetic data.

### 3.4. Inverse Method

Each fault is represented by a semi-infinite dislocation at horizontal position  $\xi_i$  slipping at a rate  $v_i$  below depth  $D_i$ . In this case, the modeled surface velocities are described by

$$\mathbf{m}_j = k_j \sum_i \left( \frac{v_i}{\pi} \right) \tan^{-1} \left( \frac{\mathbf{x} - \xi_i}{D_i} \right) \quad (1)$$

The coefficients  $k_j$  represent the projection from fault-parallel velocity to the radar LOS for each pixel; for GPS sites, the model is compared directly to the fault-parallel projection of the observed velocities so that  $k_{\text{GPS}} = 1$ .

In the heterogeneous case, we use the pre-computed elastic Green functions for each locking depth  $\mathbf{G}_i(D_i, \xi_i)$ , and the forward model is expressed as a linear combination of these functions:

$$\mathbf{m}_j = k_j \sum_i v_i \mathbf{G}_i(D_i, \xi_i). \quad (2)$$

We conducted the inversions in a Bayesian framework, which has the advantage of providing a simultaneous estimate of the parameters, their uncertainties, and their correlations (e.g., [MACKEY 2003](#); [TARANTOLA 2005](#); [MINSON \*et al.\* 2013](#)). Bayes' theorem states that the posterior probability distribution function (PDF)  $p(\mathbf{m}|\mathbf{d})$  is given by

$$p(\mathbf{m}|\mathbf{d}) \propto p(\mathbf{m})p(\mathbf{d}|\mathbf{m}), \quad (3)$$

where  $p(\mathbf{m})$  is the prior PDF and  $p(\mathbf{d}|\mathbf{m})$  is the likelihood function. The prior PDF represents our knowledge or assumptions about the model; in this case we assume a uniform prior that requires only right-lateral slip and a positive locking depth. The likelihood function is a measure of goodness of fit, defined by

$$p(\mathbf{d}|\mathbf{m}) = \frac{A}{\sqrt{|\mathbf{C}|}} \exp \left( \frac{1}{2} (\mathbf{m} - \mathbf{d})^T \mathbf{C}^{-1} (\mathbf{m} - \mathbf{d}) \right), \quad (4)$$

where  $A$  is a normalization constant,  $\mathbf{m}$  and  $\mathbf{d}$  represent the modeled and observed GPS and

InSAR velocities, and  $\mathbf{C}$  is the data covariance matrix.

The data covariance matrix  $\mathbf{C}$  represents our best information regarding the uncertainties in the input measurements, an accurate measure of which is critical for the Bayesian method to be valid. For some continuous GPS velocities, the reported one-sigma uncertainties can be very small,  $<0.1$  mm/year. These uncertainties are well justified by analyses considering a combination of white noise and flicker noise ([WILLIAMS \*et al.\* 2004](#)). However, as noted elsewhere (e.g., [PLATT and BECKER 2010](#)), attempting to fit a simplified tectonic model within these uncertainties can lead to over-fitting of the velocities, due to the presence of unmodeled tectonic or non-tectonic sources of deformation. For the diagonal entries representing the GPS uncertainties in  $\mathbf{C}$ , we, therefore, imposed a minimum value of 0.25 mm/year to avoid over-fitting continuous GPS sites with very low formal uncertainties. For the case of spatially correlated InSAR data, one may consider more realistic non-diagonal models of data covariance (e.g., [LOHMAN and SIMONS 2005](#); [SUDHAUS and JONSSON 2008](#)); however, the strain-based resampling of the InSAR significantly reduces the number of samples in non-deforming regions where unmodeled data covariance is typically a problem, so this effect should be limited. Therefore, we computed uncertainties for the resampled InSAR profile as simply the standard deviation of all data points within each resampled bin.

To ensure accurate weighting between the GPS and InSAR datasets, we further modified  $\mathbf{C}$  by re-scaling the relative GPS and InSAR uncertainties so that the two datasets make equal contributions to the total misfit value. Typically this is done by assigning empirically determined weighting factors to the two datasets (e.g., [SIMONS \*et al.\* 2002](#); [FIALKO 2004](#)); here we make use of the Bayesian formulation of the problem to determine the ideal weights exactly. In general, any part of Eq. (4) may be treated as a free parameter in the inversion, including parts of the matrix  $\mathbf{C}$ . For the case of two datasets containing  $N_1$  and  $N_2$  data points, and with unknown weights  $\gamma_1$  and  $\gamma_2$ , we can decompose Eq. (4) as the product of two likelihood functions:

$$p(\mathbf{d}|\mathbf{m}) \propto \frac{1}{\gamma_1^{N_1}} \exp\left(\frac{1}{2\gamma_1^2}(\mathbf{m}_1 - \mathbf{d}_1)^T \mathbf{C}_1^{-1}(\mathbf{m}_1 - \mathbf{d}_1)\right) \times \frac{1}{\gamma_2^{N_2}} \exp\left(\frac{1}{2\gamma_2^2}(\mathbf{m}_2 - \mathbf{d}_2)^T \mathbf{C}_2^{-1}(\mathbf{m}_2 - \mathbf{d}_2)\right). \quad (5)$$

If  $\gamma_1$  and  $\gamma_2$  are then treated as free parameters, the best-fitting values will be those for which the two datasets contribute an equal amount to the overall likelihood function. In addition, the  $\chi^2/d.o.f$  ( $\chi^2$  per degree of freedom) statistic will be close to unity, ensuring that the reported parameter uncertainties are scaled appropriately (although this limits the use of this statistic for determining which model provides a better fit to the data). This is similar to the method of FUKUDA and JOHNSON (2010), except that we do not require assumptions regarding the analytic form of the likelihood function for linear parameters. For the GPS and InSAR datasets, we found the best-fitting weights in a preliminary inversion (2.3 and 0.7, respectively), then fixed them at these values for all models. In fact, inversions using each dataset independently result in best-fitting fault parameters that are compatible within the uncertainty, so that this relative weighting is not critical to the values of the inferred parameters.

Several parameters in Eqs. (1) and (2) enter in a nonlinear manner, prohibiting a straightforward solution by least squares. Instead, we seek a distribution of models that is proportional to the posterior PDF (3). Sample models were generated using the “slice sampling” Monte Carlo technique, a computationally efficient relative of Gibbs sampling (NEAL 2003; MACKAY 2003). As with all Markov chain Monte Carlo methods, a single random walk may become trapped if there are several widely separated misfit minima, so we combined the results of a large number of walks to form the final distribution. From this distribution we may compute the means, standard deviations, and covariances between the model parameters, as well as any desired marginal posterior PDFs.

### 3.5. Fault Geometry

Models of this part of the SAF system suggest that, in addition to the SAF and SJF, contributions from

other major faults, such as the Elsinore fault (ELS) and Eastern California Shear zone (ECSZ) need to be accounted for to fit the geodetic data. These faults are subparallel to the main two, and trend northwest at an average azimuth of 310°–320°. In this area, 2D geodetic models assuming infinitely long faults (e.g., FAY and HUMPHREYS 2005; PLATT and BECKER 2010) have inferred slip rates and locking depths in good agreement with more complex 3D models (e.g., MEADE and HAGER 2005; SMITH-KONTER *et al.* 2011). Our preliminary modeling of the San Jacinto fault geometry suggested that 3D effects such as a gradually changing locking depth along strike may produce a small fault-normal component of motion, but do not produce a measurable change in the inferred locking depth or peak fault-parallel strain rate across the fault, which is our primary concern here.

Therefore, we chose a simplified model with four dislocations in a 2D elastic half-space, as shown in Fig. 1b. Previous work has shown that dislocation models of this type are extremely sensitive to the assumed fault geometry (LINDSEY and FIALKO 2013), so we initially included the horizontal positions  $\xi_i$  as free parameters in the model, then fixed them at the best-fitting locations to prevent trade-off with the other parameters. This approach is similar to the iterative procedure adopted by PLATT and BECKER (2010).

In the final model geometry, the best-fitting SAF location is offset by 6 km to the northeast of the surface trace, suggesting that the SAF dips northeast at 50°–60°, in good agreement with earlier modeling results (FIALKO 2006; LINDSEY and FIALKO 2013) as well as with seismic and other geophysical observations (LIN *et al.* 2007; FUIS *et al.* 2012). The best-fitting SJF location is offset 2 km to the northeast from its surface trace, suggesting it may also be steeply dipping to the northeast at 80°–85°. This is in good agreement with the asymmetric location of seismicity at depth and with the geometry of inferred seismic waveguide structures (LI and VERNON 2001; LEWIS *et al.* 2005) as well as with geologic observations at nearby surface exposures of the fault (DOR *et al.* 2006). Because of the very high strain rate across the SJF and the high density of geodetic data, the model is unusually sensitive to the location of this fault. We found that placing the dislocation directly

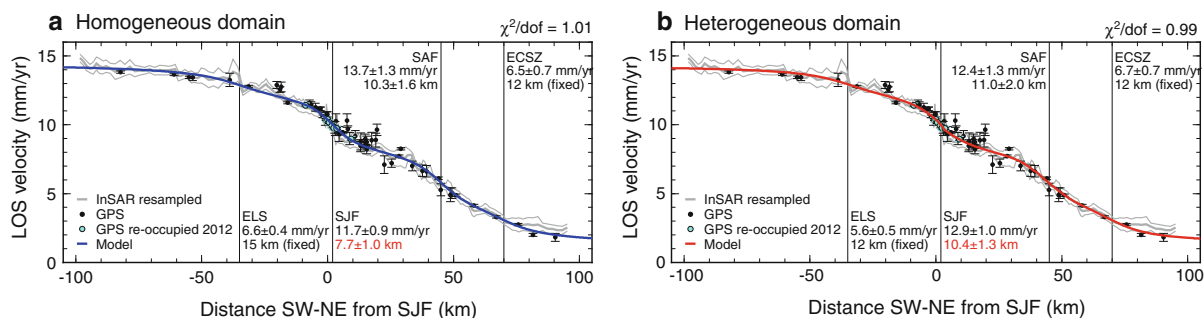


Figure 4

Dislocation model predictions compared to regional geodetic data, projected onto the radar LOS. **a** Best-fitting model in a homogeneous domain. **b** Best-fitting model in the heterogeneous domain shown in Fig. 3a. This case predicts a slightly deeper SJF locking depth, although the two models are visually indistinguishable

below the mapped fault trace can lead to an instability in the Monte Carlo inversion procedure which results in an unreasonably small SJF velocity ( $<10$  mm/year), compensated by a large velocity on the SAF (as high as 30 mm/year, the upper limit of our uniform prior PDF). This is similar to the findings of FUKUDA and JOHNSON (2010), who reported a best-fitting velocity as high as 37 mm/yr on the Coachella segment of the SAF, more than twice the geologic slip rate—a result which we suggest may have been caused by their assumptions regarding the SJF geometry.

### 3.6. Results

In the case of a homogeneous elastic half-space, the best-fitting model is shown in Fig. 4a. The inferred slip rates are  $11.7 \pm 0.9$  mm/year for the SJF,  $13.7 \pm 1.3$  mm/year for the SAF,  $6.6 \pm 0.4$  mm/year for the Elsinore, and  $6.5 \pm 0.7$  mm/year for the ECSZ. These rates, although not the primary focus of this study, are in excellent agreement with geologic slip rate estimates for each of these faults or fault zones (ROCKWELL *et al.* 1990; PETERSEN and WESNOUSKY 1994; VAN DER WOERD *et al.* 2006; BEHR *et al.* 2010; OSKIN *et al.* 2007). The best-fitting SAF locking depth is  $10.3 \pm 1.6$  km, in good agreement with the depth of seismicity on that fault. The inferred SJF locking depth of  $7.7 \pm 1.0$  km is shallow compared to the 14–18 km maximum depth of seismicity near Anza, although it is in good agreement with previous geodetic models of the area (LISOWSKI *et al.* 1991; BECKER *et al.* 2005; LUNDGREN *et al.* 2009; PLATT and BECKER 2010); the small

locking depth is required to fit the high near-fault strain rate. Although this parameter trades off strongly with the SJF slip rate (correlation  $-0.92$ ) as well as with the other model parameters (Fig. 5), it appears unlikely that a bias in these values is leading to under-estimation of the SJF locking depth because the other parameters are in good agreement with geologic, seismic, and previous geodetic results.

In the heterogeneous case, we inverted the geodetic data using the Green functions computed for the domain shown in Fig. 3a, using the same fault geometry as in the homogeneous half-space. The results are shown in Fig. 4b; the model fit to the data is visually indistinguishable from the homogeneous case. The best-fitting parameters deviate only slightly from the homogeneous case, except for the SJF locking depth which is increased by 35 % to  $10.4 \pm 1.3$  km, still significantly smaller than the depth of seismicity. This value exceeds that of the homogeneous case by more than two standard deviations, so it is clear that the elastic properties of the crust have a significant effect on this parameter. Part of this increase may be attributed to the layered nature of the rigidity structure, which causes the surface deformation pattern to become narrower compared to the homogeneous case (SAVAGE 1998). For comparison, we conducted an inversion using Green functions computed in a laterally homogeneous, horizontally averaged rigidity structure, in which case the best-fitting SJF locking depth was  $8.5 \pm 1.1$  km. Thus, the layered nature of the rigidity structure accounts for approximately 25 % of the total increase in the inferred locking depth, with the

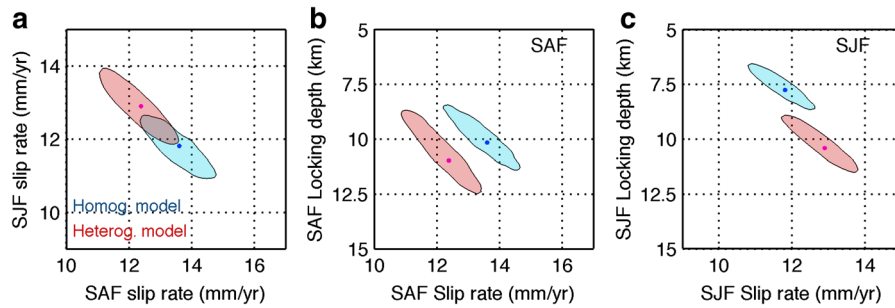


Figure 5

$1\sigma$  confidence intervals of the two-dimensional marginal posterior probability distributions showing tradeoffs between **a** SAF and SJF slip rates, **b** SAF slip rate and locking depth, and **c** SJF slip rate and locking depth, for a homogeneous (blue) and heterogeneous (red) domain

remaining 75 % attributed to the presence of the shallow compliant zone.

#### 4. Variation in Fault Locking with Depth

Geodetic locking depths in Southern California have been found to agree with the maximum depth of microseismicity in nearly all cases (SMITH-KONTER *et al.* 2011; LINDSEY and FIALKO 2013), despite the nonphysical nature of an abrupt transition from locked to sliding in dislocation models. Thus, while the true slip rate likely varies more smoothly with depth, it appears that the transition is typically centered near the bottom of the seismogenic zone, which is the depth where frictional properties transition from unstable velocity-weakening behavior to stable velocity-strengthening.

It has been proposed that the anomalous surface strain rate across the SJF (and small inferred locking depth) represents an upward extension of creep into the nominally unstable region, so that the maximum depth of microseismicity is not a good indicator of the depth of locking (WDOWINSKI 2009). This may be possible if the frictional properties of the fault interface are highly heterogeneous, with a large fraction of the interface undergoing stable creep. The observed microseismicity could then occur within small patches or lineaments of unstable velocity-weakening material, similar to the behavior observed on the creeping section of the SAF near Parkfield (RUBIN *et al.* 1999; WALDHAUSER *et al.* 2004), where it occurs at the boundary of the seismogenic zone (BARBOT *et al.* 2012). A hallmark of this scenario is the presence of repeating earthquakes, a set of seismically similar

events that occur on isolated locked asperities within the creeping fault and have a characteristic magnitude and recurrence interval (NADEAU *et al.* 1995; NADEAU and JOHNSON 1998; CHEN and LAPUSTA 2009). Preliminary evidence suggests such events may be occurring at a depth of 12–15 km along the SJF (Taira and Burgmann, pers. comm.), so that low fault coupling within the zone of active microseismicity may be an important contributor to the surface strain rate.

To quantify the effect of creep within the seismogenic zone on the geodetic data, we consider two models that relax the assumption of a sharp transition between locked and freely sliding. As above, we use the Green functions  $\mathbf{G}(D)$  determined for the heterogeneous elastic structure shown in Fig. 3a.

Rather than assuming a single locking depth  $D$ , a more realistic model would allow the slip rate to increase gradually from zero from the full rate  $v_0$  between depths  $D_1$  and  $D_2$ . The surface displacements are given by the superposition of a series of dislocations of varying slip rate  $\dot{s}(z)$ :

$$v(x) = \sum_{i=0}^N \Delta \dot{s}_i \mathbf{G}(D_1 + i\Delta z), \quad N = \frac{D_2 - D_1}{\Delta z}. \quad (6)$$

where we use  $\Delta z = 0.1$  km, the depth resolution of the pre-computed Green functions.  $\Delta \dot{s}_i$  is the change in slip rate between two neighboring steps,

$$\Delta \dot{s}_i = \dot{s}(D_1 + (i + 1)\Delta z) - \dot{s}(D_1 + i\Delta z).$$

We consider two slip rate profiles with depth: linear and elliptical. In the first case, slip rate increases linearly from zero at depth  $D_1$  to  $v_0$  at  $D_2$  so that  $\Delta \dot{s} = v_0/(N + 1)$ , a constant. The elliptical profile is designed to match more closely the predicted

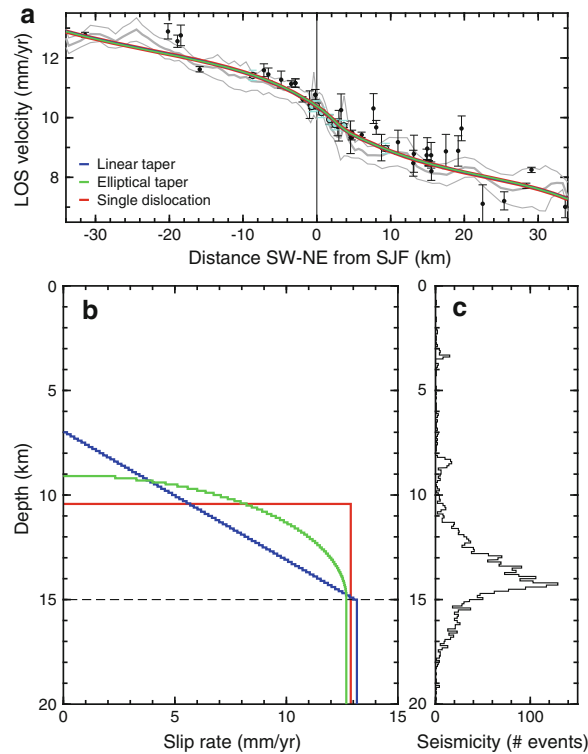


Figure 6

Comparison of three models in a heterogeneous domain. At the surface, the three models are geodetically indistinguishable (a), despite different assumptions regarding locking at depth (b). For comparison, c shows histogram of seismicity occurring within 3 km of the fault and 10 km of the center of the geodetic profile, between 1981 and 2011 (HAUKSSON *et al.* 2012)

profile of slip in numerical models incorporating rate-state friction (e.g., TSE and RICE 1986; LAPUSTA *et al.* 2000), and mimics a nearly constant stressing rate with depth within the transition zone. In this case,  $\Delta s_i$  is defined by:

$$\Delta s_i = \sqrt{1 - \frac{(D_2 - D_1 - (i+1)\Delta z)^2}{(D_2 - D_1)^2}} \sqrt{1 - \frac{(D_2 - D_1 - i\Delta z)^2}{(D_2 - D_1)^2}}. \quad (7)$$

These slip distributions are meant only to illustrate the effect of (unknown) details of slip in the transition zone on the geodetic data and moment accumulation rate. We fix  $D_2 = 15$  km in both cases so that, as in the single dislocation model, the models have only two free parameters ( $v_0$  and  $D_1$ ).

For the linear profile, the best-fitting values are  $v_0 = 13.1 \pm 0.8$  mm/year and  $D_1 = 7.0 \pm 1.8$  km; for the elliptical profile  $v_0 = 12.7 \pm 1.1$  mm/year

and  $D_1 = 9.1 \pm 1.6$  km. These results are summarized in Fig. 6. Note that the predicted surface velocities are indistinguishable (Fig. 6a) although both slip rate profiles vs. depth are significantly different from the single dislocation model (Fig. 6b). This is in good agreement with results obtained by KING and WESNOUSKY (2007), who showed that tapered or discrete coseismic slip distributions can produce virtually identical surface deformation.

For each model, we can compare the rate of moment released by creep above 15 km depth to the cumulative seismic moment of earthquakes in the same depth interval. The moment released by creep per unit length along the fault is given by

$$\frac{\Delta M_{\text{creep}}}{L} = \int_0^{D_2} \mu(z) s(z) dz, \quad (8)$$

where  $\mu$  is the seismically inferred shear modulus in Fig. 3a, and  $s$  is the total modeled slip over a given

time period. For the single dislocation model, the moment released by stable creep above 15 km over a 30-year time period would be  $6.9 \times 10^{16}$  N m/km, equivalent to a magnitude 6.0 earthquake over a 20 km-long segment of the fault. For the linear taper of slip with depth, the moment release is  $6.3 \times 10^{16}$  N m/km, and for the elliptical profile it is  $6.8 \times 10^{16}$  N m/km. In comparison, the total moment released by microseismicity recorded within 5 km of the fault, averaged over a 50 km-long segment of the SJF centered at Anza over the same time period was  $1.5 \times 10^{16}$  N m/km, based on the catalog of HAUKSSON *et al.* (2012). This average includes the high rates of seismic activity in the trifurcation and Hot Springs fault areas to the south and north of the Anza seismic gap, respectively. Even so, the seismic contribution is just 20–25 % of the total moment release required by the slip models, implying that significant frictional heterogeneity is required to support this explanation for the observed strain rate. For comparison, WDOWINSKI (2009) determined a seismic release rate equivalent to <1 mm/year of displacement along the lower 6 km of the central SJF, or 3–4 mm/year in the more seismically active area south of Anza. These rates are similar to our results, which are equivalent to 2–3 mm/year of cumulative displacement in the deep section of the fault.

### 5. Additional Elastic Modulus Reduction

Alternately, we may consider how large a reduction in shear modulus within a compliant fault zone near the surface could fully account for the strain rate while allowing a locking depth consistent with the depth of seismicity. Because of the computational effort required to evaluate Green functions in a heterogeneous domain, incorporation of the material properties as parameters in the inversion would be prohibitive. Instead, we make use of an analytic solution for the deformation due to a half-elliptical inclusion in an elastic half space (MAHRER 1981).

Consider an infinitely long half-elliptical inclusion with depth  $a$ , half-width  $b$  and shear modulus  $\mu_{in}$  embedded in a half space with shear modulus  $\mu_0$ , as shown in Fig. 7a. MAHRER (1981) showed that for the case of simple shear, the strain rate within the ellipse is

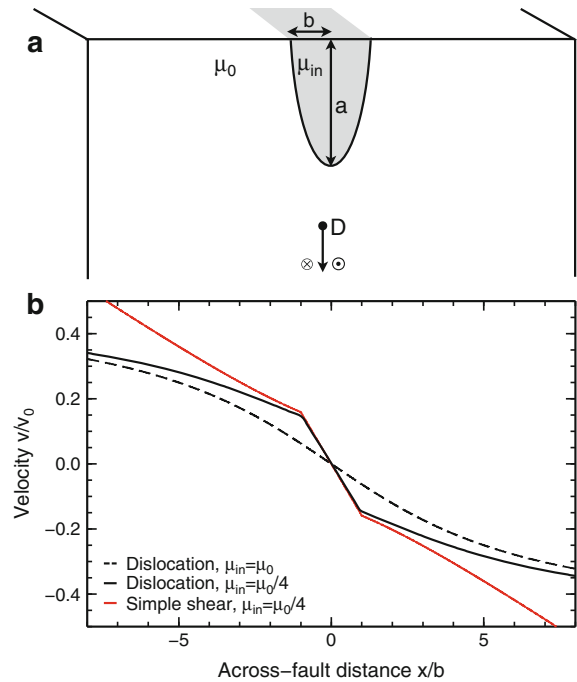


Figure 7

**a** Geometry of an elliptical inclusion in an elastic half space. **b** Comparison of the analytic solution for an elliptical inclusion under simple shear (red) (MAHRER 1981) with the numerical result for a dislocation below the elliptical inclusion (black), and a dislocation in a homogeneous elastic half space (dashed). Parameters are  $a = 3b$ ,  $\mu_{in} = \mu_0/4$ , and dislocation locking depth  $D = 5b$

$$\dot{\epsilon}_{xy} = \frac{\sigma_0/\mu_0(1 + \phi)}{1 + \phi/r}, \quad (9)$$

where  $\phi = a/b$  and  $r = \mu_0/\mu_{in}$ . If the locking depth is much greater than the depth of the compliant zone, then the strain rate is nearly constant within the zone and may be approximated by simple shear. The validity of this assumption is demonstrated in Fig. 7b, by comparison of the analytic solution with the numerical result for a buried dislocation beneath the same elliptical inclusion. Although the boundary conditions are different, the strain rate within the inclusion predicted by Eq. (9) is in excellent agreement with the numerical result. Alternative models are possible; JOLIVET *et al.* (2009) addressed a similar question on the northern SAF using the analytic solution for a dislocation below a rectangular inclusion in a half space. In this case, we feel the elliptical inclusion provides a better approximation to the observed geometry of the fault zone (see Fig. 3a).

Table 2

Required shear modulus ratio for varying compliant fault zone depths, computed using Eq. (10) taking the half-width  $b = 1.5\text{km}$  and strain enhancement ratio  $f = 2.4$

Compliant zone depth (km)	Aspect ratio $\phi$	$\mu_0/\mu_{in}$
3	2	8.0
6	4	3.7
9	6	3.1
12	8	2.9
15	10	2.8
$\infty$	$\infty$	2.4

Relative to a homogeneous half-space, Eq. (9) predicts that the strain rate is enhanced within the compliant zone by a factor  $f = (1 + \phi)/(1 + \phi/r)$ . Given a measurement of the near-field strain rate enhancement and the dimensions of the inclusion, we can directly solve for the shear modulus ratio:

$$r = \frac{\phi f}{1 + \phi - f}. \quad (10)$$

In the case of the SJF, the strain rate recorded by the GPS data within the fault zone is  $0.60 \pm 0.1 \mu\text{rad/yr}$ . If the fault is locked at 15 km and slipping at a rate of 12 mm/year, the predicted strain rate would be  $\epsilon_{xy} = v/\pi D = 0.25 \mu\text{rad/yr}$  in a homogeneous half space. The required strain rate enhancement is, therefore,  $f = 2.4$ , and we take the fault zone half-width  $b = 1.5$  km. The remaining unknown parameter is the compliant zone depth  $a$ . From Eq. (10) it may be seen that depths  $< 2.1$  km, which result in an aspect ratio  $< 1.4$ , cannot produce the required strain rate even if the shear modulus in the fault zone is zero. We consider a range of larger depths in Table 2; if the zone is infinitely deep, Eq. (10) reduces to the case of a vertical compliant layer (RYBICKI and KASAHARA 1977), in which case a shear modulus reduction by a factor of 2.4 would be required. The tomographic results (Fig. 3a) and theoretical models of damage due to dynamic earthquake ruptures (e.g., KANEKO and FIALKO 2011) do not support a deep low rigidity zone, and for smaller depths the required degree of reduction in shear modulus (a factor of three or more) does not appear to be physically plausible if the material behaves elastically, given the range of properties observed for crustal materials.

## 6. Discussion

Early geodetic surveys across the San Jacinto fault at Anza suggested an unusually high rate of interseismic strain accumulation across the fault, although these observations were subject to significant uncertainties (LISOWSKI *et al.* 1991). The combination of updated campaign GPS and InSAR data presented here demonstrate unambiguously the presence of a zone of enhanced fault-parallel shear at Anza (Fig. 1c). The maximum shear strain rate determined from GPS is  $0.60 \pm 0.1 \mu\text{rad/year}$  across a 3 km-wide zone, asymmetrically offset to the northeast of the fault trace. The InSAR results (MANZO *et al.* 2011) suggest a higher strain rate of  $0.79 \mu\text{rad/year}$  (Fig. 1c). These values are approximately twice the strain rate in the neighboring crust to either side of the fault, giving rise to an unrealistically small predicted locking depth when interpreted with a dislocation model in a homogeneous elastic half space (Fig. 4a). We have considered three potential mechanisms that might explain this behavior: shallow fault creep, a reduced effective elastic modulus within a fault damage zone, or occurrence of steady creep in the lower part of the seismogenic zone.

In the first case, GPS occupations of the Mitchell road alignment array at Anza allow us to rule out shallow, localized fault creep as a contributor to the high gradients in the surface velocity field (Fig. 2). The 20-year timespan of the measurements provides an accuracy of 0.2 mm/year, a significant improvement over earlier results (LOUIE *et al.* 1985). The lack of observable creep stands in contrast with models of earthquake cycle governed by rate- and state-dependent friction laws, which predict that the upper several kilometers of mature strike-slip faults should undergo stable creep in the late interseismic period, even if the material is velocity-weakening (MARONE and SCHOLZ 1988; SCHOLZ 1998; TSE and RICE 1986; LAPUSTA *et al.* 2000; KANEKO *et al.* 2013). One possibility is that the local state of stress is transpressional, so that increased normal stress on the fault may help suppress shallow creep.

Second, the anomalous strain may be attributed to a reduced shear modulus within a compliant fault zone. Zones of this type, extending up to several

kilometers from the fault, have been inferred in several cases, based on both geodetic (RYBICKI and KASAHARA 1977; LISOWSKI *et al.* 1991; FIALKO *et al.* 2002; CHEN and FREYMUELLER 2002; FIALKO 2004; HAMIEL and FIALKO 2007; JOLIVET *et al.* 2009; ÇAKIR *et al.* 2012) and seismic evidence (SPUDICH and OLSEN 2001; COCHRAN *et al.* 2009; LEWIS *et al.* 2005). Depending on the magnitude of shear modulus reduction and the geometry of the zone, the near-fault strain rate may be significantly increased. A massive low-velocity zone has been imaged along the SJF at Anza by seismic tomography (ALLAM and BEN-ZION 2012). Additionally, the zone of elevated strain rate is asymmetric with respect to the fault (Fig. 1c), consistent with observations of asymmetric damage inferred from geologic observations and LiDAR-derived drainage density maps (DOR *et al.* 2006; WECHSLER *et al.* 2009) and dynamic rupture models which predict asymmetric damage arising from preferred rupture directivity (e.g., BEN-ZION and SHI 2005; AMPUERO and BEN-ZION 2008).

We computed surface velocities due to dislocations in a half-space with elastic properties inferred from seismic tomography (ALLAM and BEN-ZION 2012), and found that the observed shear modulus reduction of 20–40 % does contribute significantly to the near-fault strain rate (Fig. 3), resulting in an increase of the best-fitting locking depth by 35 %, to  $10.4 \pm 1.3$  km (Fig. 4b). However, if the fault is locked to 15 km as expected from the distribution of microseismicity (HAUKSSON *et al.* 2012), the shear modulus would have to be reduced by a factor of 2.4 or more within the compliant fault zone (Table 2) to explain the geodetic data, a contrast that is too high given available seismic observations.

One mechanism that might contribute to the enhanced strain rate is a reduced yield strength within the fault zone, leading to unrecoverable plastic deformation, or distributed slip on a large number of subparallel fault strands. In addition to the seismically observed compliant zone, such yielding could result in a much smaller apparent shear modulus from the geodetic perspective. Some form of inelastic yielding has been suggested as an explanation for the shallow slip deficit observed during large ( $M \sim 7$ ) strike-slip earthquakes in southern California as well as other regions (SIMONS

*et al.* 2002; FIALKO *et al.* 2005; KANEKO and FIALKO 2011). If this yielding persists throughout much of the interseismic period, the accumulation of unrecoverable strain could have significant implications for geologic slip rates, the state of crustal stress, and consequently the seismic hazard. Alternately, yielding might occur only toward the end of the interseismic period when the highest stresses are reached, in which case it would account for a comparatively small amount of the total strain. Addressing this question will require geodetic data of comparable density and accuracy across a number of faults of different maturity and at different points in the seismic cycle, and an improved knowledge of the effects of both coseismic damage and interseismic healing on the material yield strength over time.

Another possibility, proposed by WADOWSKI (2009), is that the elevated surface strain rate arises from deep interseismic creep extending into the nominally unstable zone above 15 km depth. Such an upward extension of creep is predicted by rate and state frictional models late in the earthquake cycle, if the critical slip-weakening distance is assumed to be much larger than laboratory estimates suggest (e.g., TSE and RICE 1986; LAPUSTA *et al.* 2000). In these models, accelerated aseismic creep propagates into the velocity-weakening layer until the conditions for nucleation of seismic rupture are met (SCHOLZ 1998). In some cases, models with a large slip-weakening distance predict creep within the seismogenic zone at a significant fraction of the interseismic rate (LAPUSTA and RICE 2003). However, SAVAGE (2006) found that the maximum surface strain rate in frictionally controlled models of deep slip should be less than that predicted by a dislocation model that is fully locked within the seismogenic zone, even for amplitudes of creep within the deep part of the seismogenic zone reaching one-third of the total fault slip rate. In such cases, the slip-weakening distance is large enough that the resulting nucleation size required for seismic rupture would prohibit the occurrence of microseismicity on the fault plane, unless there is significant frictional heterogeneity.

The presence of frictional heterogeneity on this segment of the SJF could allow for both active microseismicity and large areas of stable creep,

possibly at a rate high enough to impact the surface strain rate. However, it should also lead to qualitatively different microseismic behavior such as repeating earthquakes and well defined spatial patterns of seismicity, such as observed along the SAF near Parkfield (NADEAU *et al.* 1995; RUBIN *et al.* 1999; WALDHAUSER *et al.* 2004). At present, microseismic behavior of this type has not been conclusively observed, although preliminary studies suggest that repeating events may in fact be occurring (Taira and Burgmann, pers. comm.), so this explanation for the elevated strain rate may merit further consideration.

To constrain better the rate and depth distribution of deep creep under this interpretation, we considered two tapered slip rate profiles in addition to the simplified single dislocation model, shown in Fig. 6. The sensitivity of the geodetic data to the details of the slip distribution at the base of the seismogenic zone is nearly zero, although the total moment release rate is well constrained. Thus, all of the models require significant ongoing moment release above the apparent frictional stability transition at  $\sim 15$  km at a rate equivalent to 4–6 times the total moment released as microseismicity within this zone over the past 30 years. The effective aseismic moment released by such creep would be equivalent to a magnitude 6.0 earthquake every 30 years within a 20 km-long segment. Under this interpretation, the best-fitting geodetic locking depth of  $10.4 \pm 1.3$  km reflects an accurate measure of the depth of strain accumulation and potential future moment release that is significantly different from the depth inferred from seismic observations alone.

Finally, we note that uncertainties in the fault geometry and the presence of other active faults may further modify the results. For example, the Earthquake Valley fault located 25 km southwest of the SJF is not typically considered in geodetic models of the region, but recent geologic evidence suggests that it may slip at a long-term rate of 2–3 mm/year (ROCKWELL *et al.* 2013). If one includes this fault in the above models, the best-fitting SJF locking depth increases to  $11.1 \pm 0.8$  km. This would slightly reduce the potential contributions of inelastic yielding and/or heterogeneous frictional properties discussed above.

## 7. Conclusions

New geodetic observations confirm a relatively narrow (2–3 km wide) zone with an elevated rate of shear strain across the San Jacinto fault at Anza. We have shown that a reduced elastic shear modulus within the fault zone as inferred by seismic tomography can explain a significant part of the elevated strain rate but cannot fully account for the small locking depths inferred using dislocation models. We ruled out the presence of shallow creep via the re-occupation with GPS of an alignment array installed at Anza in 1990. There are two remaining interpretations of the elevated strain rate: additional elastic or unrecoverable inelastic yielding occurring within the shallow fault zone, or significant stable creep within the deep part of the seismogenic zone. The first explanation, if confirmed, would have significant implications for geologically inferred slip rates and hazard assessment on this and other mature crustal faults, as yielding during the interseismic period would reduce the cumulative coseismic offsets expressed on the fault trace. Such behavior would also affect the state of stress in the crust and the subsequent coseismic release of strain energy. This hypothesis predicts that inelastic deformation and an increased shear strain rate should be geodetically observable in the vicinity of other active faults which are approaching the end of the interseismic period. Alternately, stable creep within the deep part of the fault zone could explain the geodetic strain rate, but requires the presence of significant frictional heterogeneity. Such creep, if present, would represent approximately four to six times more moment release than the observed microseismicity, indicating that the deep part of the seismogenic zone is predominantly velocity-strengthening.

## Acknowledgments

This work was supported by NSF (grant EAR-0908042) and SCEC. The authors would like to acknowledge Duncan Agnew, Peng Fang and Robert King for their invaluable assistance with the GPS data processing. The original installment of the survey monuments was supported by NSF grant EAR-9104810.

## REFERENCES

- ALLAM AA, BEN-ZION Y (2012) *Seismic velocity structures in the southern California plate-boundary environment from double-difference tomography*. *Geophys J Int* 190(2):1181–1196. doi:10.1111/j.1365-246X.2012.05544.x
- AMPUERO JP, BEN-ZION Y (2008) *Cracks, pulses and macroscopic asymmetry of dynamic rupture on a bimaterial interface with velocity-weakening friction*. *Geophys J Int* 173:674–692. doi:10.1111/j.1365-246X.2008.03736.x
- BARBOT S, FIALKO Y, SANDWELL D (2009) *Three-dimensional models of elasto-static deformation in heterogeneous media, with applications to the Eastern California Shear Zone*. *Geophys J Int* 179:500–520
- BARBOT S, LAPUSTA N, AVOUAC J-P (2012) *Under the Hood of the Earthquake Machine: Toward Predictive Modeling of the Seismic Cycle*. *Science* 336:707–710. doi:10.1126/science.1218796
- BECKER TW, HARDEBECK JL, ANDERSON G (2005) *Constraints on fault slip rates of the Southern California plate boundary from GPS velocity and stress inversions*. *Geophys J Int* 160:634–650. doi:10.1111/j.1365-246X.2004.02528.x
- BEHR WM, ROOD DH, FLETCHER KE, GUZMAN N, FINKEL R, HANKS TC, HUDNUT KW, KENDRICK KJ, PLATT JP, SHARP WD, J WR, YULE RJ (2010) *Uncertainties in slip-rate estimates for the Mission Creek strand of the southern San Andreas fault at Biskra Palms Oasis, southern California*. *Geol Soc Am Bull* 122:1360–1377. doi:10.1130/B30020.1
- BEN-ZION Y, PENG Z, OKAYA D, SEEBER L, ARMBRUSTER J, OZER N, MICHAEL A, BARIS S, AKTAR M, KUWAHARA Y, ITO H (2003) *A shallow fault-zone structure illuminated by trapped waves in the Karadere-Duzce branch of the North Anatolian Fault, western Turkey*. *Geophys J Int* 152:699–699. doi:10.1046/j.1365-246X.2003.01870.x
- BEN-ZION Y, SHI Z (2005) *Dynamic rupture on a material interface with spontaneous generation of plastic strain in the bulk*. *Earth Planet Sci Lett* 236:486–496. doi:10.1016/j.epsl.2005.03.025
- BLISNIUK K, ROCKWELL T, OWEN LA, OSKIN M, LIPPINCOTT C, CAFFEE MW, DORTCH J (2010) *Late Quaternary slip rate gradient defined using high-resolution topography and <sup>10</sup>Be dating of offset landforms on the southern San Jacinto Fault zone, California*. *J Geophys Res* 115:B08401. doi:10.1029/2009JB006346
- BOCK Y, NIKOLAIDIS RM, DE JONGE PJ (2000) *Instantaneous geodetic positioning at medium distances with the Global Positioning System*. *J Geophys Res* 105:28,223–28,253
- BROCHER TM (2005) *Empirical relations between elastic wavespeeds and density in the earth's crust*. *Bulletin of the Seismological Society of America* 95(6). doi:10.1785/0120050077
- CAKIR Z, ERGINTAV S, OZENER H, DOGAN U, AKOGLU AM, MEGHRAOUI M, REILINGER R (2012) *Onset of aseismic creep on major strike-slip faults*. *Geology* 40:1115–1118. doi:10.1130/G33522.1
- CHEN Q, FREYMUELLER J (2002) *Geodetic evidence for a near-fault compliant zone along the San Andreas fault in the San Francisco Bay area*. *Bull Seismol Soc Am* 92:656–671
- CHEN T, LAPUSTA N (2009) *Scaling of small repeating earthquakes explained by interaction of seismic and aseismic slip in a rate and state fault model*. *J Geophys Res* 114:B01311. doi:10.1029/2008JB005749
- CLEVELAND WS (1979) *Robust locally weighted regression and smoothing scatterplots*. *J Am Statist Assoc* 74:829–836. doi:10.2307/2286407
- CLEVELAND WS, DEVLIN SJ (1988) *Locally-weighted regression: An approach to regression analysis by local fitting*. *J Am Statist Assoc* 83:596–610. doi:10.2307/2289282
- COCHRAN ES, LI YG, SHEARER PM, BARBOT S, FIALKO Y, VIDALE JE (2009) *Seismic and geodetic evidence for extensive, long-lived fault damage zones*. *Geology* 37:315–318. doi:10.1130/G25306A.1
- DOR O, ROCKWELL TK, BEN-ZION Y (2006) *Geological observations of damage asymmetry in the structure of the san jacinto, san andreas and punchbowl faults in southern california: A possible indicator for preferred rupture propagation direction*. *Pure appl geophys*. 163:301–349. doi:10.1007/s00024-005-0023-9
- FAY N, HUMPHREYS G (2005) *Fault slip rates, effects of elastic heterogeneity on geodetic data, and the strength of the lower crust in the Salton Trough region, southern California*. *J Geophys Res* 110:B09401. doi:10.1029/2004JB003548
- FIALKO Y (2004) *Probing the mechanical properties of seismically active crust with space geodesy: Study of the co-seismic deformation due to the 1992 M<sub>w</sub>7.3 Landers (southern California) earthquake*. *J Geophys Res* 109:B03307. doi:10.1029/2003JB002756
- FIALKO Y (2006) *Interseismic strain accumulation and the earthquake potential on the southern San Andreas fault system*. *Nature* 441:968–971
- FIALKO Y, SANDWELL D, AGNEW D, SIMONS M, SHEARER P, MINSTER B (2002) *Deformation on nearby faults induced by the 1999 Hector Mine earthquake*. *Science* 297:1858–1862. doi:10.1126/science.1074671
- FIALKO Y, SANDWELL D, SIMONS M, ROSEN P (2005) *Three-dimensional deformation caused by the Bam, Iran, earthquake and the origin of shallow slip deficit*. *Nature* 435:295–299
- FUIS GS, SCHEIRER DS, LANGENHEIM VE, KOHLER MD (2012) *A new perspective on the geometry of the san andreas fault in southern california and its relationship to lithospheric structure*. *Bull Seism Soc Am* 102:236–251
- FUKUDA J, JOHNSON KM (2010) *Mixed linear-non-linear inversion of crustal deformation data: Bayesian inference of model, weighting and regularization parameters*. *Geophys J Int* 181:1441–1458. doi:10.1111/j.1365-246X.2010.04564.x
- GOULTY NR, BURFORD RO, ALLEN CR, GILMAN R, JOHNSON CE, KELLER RP (1978) *Large creep events on the Imperial Fault, California*. *Bull Seism Soc Am* 68:517–521
- HAMIEL Y, FIALKO Y (2007) *Structure and mechanical properties of faults in the North Anatolian Fault system from InSAR observations of coseismic deformation due to the 1999 Izmit (Turkey) earthquake*. *J Geophys Res* 112:B07412. doi:10.1029/2006JB004777
- HAUKSSON E, YANG W, SHEARER PM (2012) *Waveform relocated earthquake catalog for southern california (1981 to 2011)*. *Bull Seism Soc Am* 102(5):2239–2244. doi:10.1785/0120120010
- HERRING TA, KING RW, McCLUSKY SC (2010) *Introduction to GAMIT/GLOBK*. Massachusetts Institute of Technology, Cambridge, Massachusetts
- JOHNSON HO, AGNEW DC, WYATT FK (1994) *Present-day crustal deformation in southern California*. *J Geophys Res* 99:23951–23974
- JOLIVET R, BURGMANN R, HOULIE N (2009) *Geodetic exploration of the elastic properties across and within the northern San Andreas Fault zone*. *Earth Planet Sci Lett* 288:126–131. doi:10.1016/j.epsl.2009.09.014
- KANEKO Y, FIALKO Y (2011) *Shallow slip deficit due to large strike-slip earthquakes in dynamic rupture simulations with elastoplastic off-fault response*. *Geophys J Int* 186:1389–1403. doi:10.1111/j.1365-246X.2011.05117.x

- KANEKO Y, FIALKO Y, SANDWELL DT, TONG X, FURUYA M (2013) *Interseismic deformation and creep along the central section of the North Anatolian fault (Turkey): InSAR observations and implications for rate-and-state friction properties*. *J Geophys Res* 118:316–331, doi:[10.1029/2012JB009661](https://doi.org/10.1029/2012JB009661)
- KELLER RP, ALLEN CR, GILMAN R, GOULTY NR, HILEMAN JA (1978) *Monitoring slip along major faults in Southern California*. *Bull Seism Soc Am* 68(4):1187–1190
- KING GCP, WESNOUSKY SG (2007) *Scaling of fault parameters for continental strike-slip earthquakes*. *Bull Seism Soc Am* 97(6):1833–1840, doi:[10.1785/0120070048](https://doi.org/10.1785/0120070048)
- LAPUSTA N, RICE J, BEN-ZION Y, ZHENG G (2000) *Elastodynamic analysis for slow tectonic loading with spontaneous rupture episodes on faults with rate- and state-dependent friction*. *J Geophys Res* 105(B10):23,765–23,789, doi:[10.1029/2000JB900250](https://doi.org/10.1029/2000JB900250)
- LAPUSTA N, RICE J (2003) *Nucleation and early seismic propagation of small and large events in a crustal earthquake model*. *J Geophys Res* 108(B4):2205, doi:[10.1029/2001JB000793](https://doi.org/10.1029/2001JB000793)
- LEWIS MA, PENG Z, BEN-ZION Y, VERNON FL (2005) *Shallow seismic trapping structure in the san jacinto fault zone near anza, california*. *Geophys J Int* 162:867–881, doi:[10.1111/j.1365-246X.2005.02684.x](https://doi.org/10.1111/j.1365-246X.2005.02684.x)
- LI Y, VERNON FL (2001) *Characterization of the san jacinto fault zone near anza, california, by fault zone trapped waves*. *J Geophys Res* 106:30,671–30,688, doi:[10.1029/2000JB000107](https://doi.org/10.1029/2000JB000107)
- LIN G, SHEARER PM, HAUSSON E (2007) *Applying a three-dimensional velocity model, waveform cross correlation, and cluster analysis to locate southern California seismicity from 1981 to 2005*. *J Geophys Res* 112:B12309, doi:[10.1029/2007JB004986](https://doi.org/10.1029/2007JB004986)
- LINDSEY EO, FIALKO Y (2013) *Geodetic slip rates in the southern San Andreas fault system: effects of elastic heterogeneity and fault geometry*. *J Geophys Res* 118, doi:[10.1029/2012JB009358](https://doi.org/10.1029/2012JB009358)
- LISOWSKI M, SAVAGE J, PRESCOTT WH (1991) *The velocity field along the San Andreas fault in central and southern California*. *J Geophys Res* 96:8369–8389
- LOHMAN RB, SIMONS M (2005) *Some thoughts on the use of InSAR data to constrain models of surface deformation: Noise structure and data downsampling*. *Geochem Geophys Geosyst* 6, doi:[10.1029/2004GC000841](https://doi.org/10.1029/2004GC000841)
- LOUIE JN, ALLEN CR, JOHNSON DC, HAASE PC, COHN SN (1985) *Fault slip in Southern California*. *Bulletin of the Seismological Society of America* 75(3):811–833
- LUDWIG WJ, NAFE JE, DRAKE CL (1970) *Seismic refraction*. In: Maxwell AE (ed) *The Sea*, vol 4, Wiley-Interscience, New York, pp 53–84
- LUNDGREN PE, HETLAND A, LIU Z, FIELDING EJ (2009) *Southern San Andreas–San Jacinto fault system slip rates estimated from earthquake cycle models constrained by GPS and interferometric synthetic aperture radar observations*. *J Geophys Res* 114:B02403, doi:[10.1029/2008JB005996](https://doi.org/10.1029/2008JB005996)
- LYONS S, SANDWELL D (2003) *Fault creep along the southern San Andreas from interferometric synthetic aperture radar, permanent scatterers, and stacking*. *J Geophys Res* 108 doi:[10.1029/2002JB001831](https://doi.org/10.1029/2002JB001831)
- LYONS SN, BOCK Y, SANDWELL DT (2002) *Creep along the Imperial fault, Southern California, from GPS measurements*. *J Geophys Res* 107, doi:[10.1029/2001JB000763](https://doi.org/10.1029/2001JB000763)
- MACKEY DJC (2003) *Information Theory, Inference, and Learning Algorithms*. Cambridge University Press, Cambridge, UK
- MAHRER KD (1981) *Surface deformation in a crustal setting with a long-surfaced non-uniformity*. *Tectonophysics* 76:T1–T11
- MANZO M, FIALKO Y, CASU F, PEPE A, LANARI R (2011) *A quantitative assessment of DInSAR measurements of interseismic deformation: the Southern San Andreas Fault case study*. *Pure Appl Geophys* doi:[10.1007/s00024-011-0403-2](https://doi.org/10.1007/s00024-011-0403-2)
- MARONE C (1998) *Laboratory-derived friction laws and their application to seismic faulting*. *Annu Rev Earth Planet Sci* 26:643–696
- MARONE C, SCHOLZ CH (1988) *The depth of seismic faulting and the upper transition from stable to unstable slip regimes*. *Geophys Res Lett* 15:621–624
- MEADE, BJ and HAGER, BH (2005) *Block models of crustal motion in southern California constrained by GPS measurements*. *J Geophys Res* 110, doi:[10.1029/2004JB003209](https://doi.org/10.1029/2004JB003209)
- MINSON SE, SIMONS M, BECK JL (2013) *Bayesian inversion for finite fault earthquake source models I theory and algorithm*. *Geophys J Int* 133:568–584, doi:[10.1093/gji/ggt180](https://doi.org/10.1093/gji/ggt180)
- NADEAU R, JOHNSON L (1998) *Seismological studies at Parkfield VI: Moment release rates and estimates of source parameters for small repeating earthquakes*. *Bull Seism Soc Am* 88:790–814
- NADEAU RM, FOXALL W, McEVILLY TV (1995) *Clustering and periodic recurrence of microearthquakes on the San Andreas fault at Parkfield, California*. *Science* 267:503–507, doi:[10.1126/science.267.5197.503](https://doi.org/10.1126/science.267.5197.503)
- NEAL RM (2003) *Slice sampling*. *Ann Stat* 31:705–767
- NUR A, MAVKO J (1974) *Postseismic viscoelastic rebound*. *Science* 183:204–206
- OSKIN M, PERG L, BLUMENTRITT D, MUKHOPADHYAY S, IRIONDO A (2007) *Slip rate of the Calico fault: Implications for geologic versus geodetic rate discrepancy in the Eastern California Shear Zone*. *J Geophys Res* 112:B03402, doi:[10.1029/2006JB004451](https://doi.org/10.1029/2006JB004451)
- PETERSEN MD, WESNOUSKY SG (1994) *Fault slip rates and earthquake histories for active faults in Southern California*. *Bull Seism Soc Am* 84:1608–1649
- PLATT JP, BECKER TW (2010) *Where is the real transform boundary in California? Geochemistry, Geophysics, Geosystems* 11, doi:[10.1029/2010GC003060](https://doi.org/10.1029/2010GC003060)
- ROCKWELL T, LOUGHMAN C, MERIFIELD P (1990) *Late quaternary rate of slip along the San-Jacinto fault zone near Anza, Southern California*. *J Geophys Res* 95:8593–8605
- ROCKWELL TK, MAGISTRALE H, HARADEN C, HIRABAYASHI CK (1992) *Emplacement of alignment arrays along the Elsinore and San Jacinto fault zones, Southern California*. *USGS Open File Rep pp Grant No. 14–08–0001–G1771*
- ROCKWELL TK, SEITZ G, DAWSON T, YOUNG J (2006) *The long record of san jacinto fault paleoearthquakes at hog lake: Implications for regional patterns of strain release in the southern san andreas fault system*. *Seismol Res Lett* 77(2):270
- ROCKWELL TK, AKCIZ SO, GORDON E (2013) *Paleoseismology of the Aqua Tibia - Earthquake Valley fault, eastern strand of the Elsinore fault zone*. *Seismol Res Lett* 84(2):332
- RUBIN AM, GILLARD D, GOT JL (1999) *Streaks of microearthquakes along creeping faults*. *Nature* 400:635–641, doi:[10.1038/23196](https://doi.org/10.1038/23196)
- RYBICKI K, KASAHARA K (1977) *A strike-slip fault in a laterally inhomogeneous medium*. *Tectonophysics* 42:127–138
- RYMER M (2000) *Triggered surface slips in the Coachella Valley area associated with the 1992 Joshua Tree and Landers, California, earthquakes*. *Bull Seism Soc Am* 90:832–848
- RYMER MJ, BOATWRIGHT J, SEEKINS LC, YULE JD, LIU J (2002) *Triggered surface slips in the Salton Trough associated with the*

- 1999 *Hector Mine, California, Earthquake*. Bull Seism Soc Am 92:1300–1317
- SANDERS CO (1990) *Earthquake depths and the relation to strain accumulation and stress near strike-slip faults in Southern California*. J Geophys Res 95:4571–4762
- SANDERS CO, KANAMORI H (1984) *A seismotectonic analysis of the Anza seismic gap, San Jacinto fault zone, Southern California*. J Geophys Res 89:5873–5890
- SAVAGE J (1998) *Displacement field for an edge dislocation in a layered half-space*. J Geophys Res 103:2439–2446
- SAVAGE J, BURFORD R (1973) *Geodetic determination of relative plate motion in central California*. J Geophys Res 78:832–845
- SAVAGE JC (1990) *Equivalent strike-slip earthquake cycles in half-space and lithosphere-asthenosphere earth models*. J Geophys Res 95:4873–4879
- SAVAGE JC (2006) *Dislocation pileup as a representation of strain accumulation on a strike-slip fault*. J Geophys Res 111:B04,405, doi:10.1029/2005JB004021
- SAVAGE JC, PRESCOTT WH (1978) *Asthenosphere readjustment and the earthquake cycle*. J Geophys Res 83:3369–3376
- SCHOLZ CH (1998) *Earthquakes and friction laws*. Nature 391:37–42, doi:10.1038/34097
- SHARP R, RYMER M, LIENKAEMPER J (1986) *Surface displacement on the Imperial and Superstition Hills faults triggered by the Westmoreland, California, earthquake of 26 April 1981*. Bull Seism Soc Am 76:949–965
- SHEN ZK, KING RW, AGNEW DC, WANG M, HERRING TA, DONG D, FANG P (2011) *A unified analysis of crustal motion in Southern California, 1970–2004: The SCEC crustal motion map*. Journal of Geophysical Research 116(B11):1–19, doi:10.1029/2011JB008549. <http://www.agu.org/pubs/crossref/2011/2011JB008549.shtml>
- SIEH K, WILLIAMS P (1990) *Behavior of the southernmost San Andreas fault during the past 300 years*. J Geophys Res 95:6629–6645
- SIMONS M, FIALKO Y, RIVERA L (2002) *Coseismic deformation from the 1999  $M_w$ 7.1 Hector Mine, California, earthquake, as inferred from InSAR and GPS observations*. Bull Seism Soc Am 92:1390–1402
- SMITH-KONTER BR, SANDWELL DT, SHEARER P (2011) *Locking depths estimated from geodesy and seismology along the san andreas fault system: Implications for seismic moment release*. J Geophys Res 116(B6):1–12, doi:10.1029/2010JB008117. <http://www.agu.org/pubs/crossref/2011/2010JB008117.shtml>
- SPUDICH P, OLSEN K (2001) *Fault zone amplified waves as a possible seismic hazard along the Calaveras fault in Central California*. Geophys Res Lett 28:2533–2536
- SUDHAUS H, JONSSON S (2008) *Improved source modelling through combined use of InSAR and GPS under consideration of correlated data errors: application to the June 2000 Kleifarvatn earthquake, Iceland*. Geophys J Int 176:389–404, doi:10.1111/j.1365-246X.2008.03989.x
- TAKEUCHI C, FIALKO Y (2012) *Dynamic models of interseismic deformation and stress transfer from plate motion to continental transform faults*. J Geophys Res 117:B05403, doi:10.1029/2011JB009056
- TARANTOLA A (2005) *Inverse Problem Theory and Methods for Model Parameter Estimation*. Society for Industrial and Applied Mathematics, Philadelphia, doi:10.1137/1.9780898717921
- THATCHER W, HILEMAN JA, HANKS TC (1975) *Seismic slip distribution along the san jacinto fault zone, southern california and its implications*. Geological Society of America Bulletin 86:1140–1146
- TONG X, SANDWELL DT, SMITH-KONTER B (2013) *High-resolution interseismic velocity data along the San Andreas Fault from GPS and InSAR*. J Geophys Res 118, doi:10.1029/2012JB009442
- TSE ST, RICE JR (1986) *Crustal earthquake instability in relation to the depth variation of frictional slip properties*. J Geophys Res 91:9452–9472
- VAN DER WOERD J, KLINGER Y, SIEH K, TAPPONNIER P, RYERSON F, MERIAUX A (2006) *Long-term slip rate of the southern San Andreas Fault from  $^{10}\text{Be}$ - $^{26}\text{Al}$  surface exposure dating of an offset alluvial fan*. J Geophys Res 111:B04407, doi:10.1029/2004JB003559
- WALDHAUSER F, ELLSWORTH WL, SCHAFF DP, COLE A (2004) *Streaks, multiplets, and holes: High-resolution spatio-temporal behavior of Parkfield seismicity*. Geophys Res Lett 31, doi:10.1029/2004GL020649
- WDOWINSKI S (2009) *Deep creep as a cause for the excess seismicity along the San Jacinto fault*. Nature Geoscience 2(12):882–885, doi:10.1038/ngeo0684
- WECHSLER N, ROCKWELL TK, BEN-ZION Y (2009) *Application of high resolution DEM data to detect rock damage from geomorphic signals along the central San Jacinto Fault*. Geomorphology 113:82–96, doi:10.1016/j.geomorph.2009.06.007
- WEI M, SANDWELL D, FIALKO Y (2009) *A silent  $M$ 4.8 slip event of October 3–6, 2006, on the Superstition Hills fault, Southern California*. J Geophys Res 114:B07402, doi:10.1029/2008JB006135
- WEI M, SANDWELL D, SMITH-KONTER B (2010) *Optimal combination of InSAR and GPS for measuring interseismic crustal deformation*. Adv Space Res 46:236–249
- WEI M, SANDWELL D, FIALKO Y, BILHAM R (2011) *Slip on faults in the Imperial Valley triggered by the 4 April 2010  $M_w$  7.2 El Mayor-Cucapah earthquake revealed by InSAR*. Geophys Res Lett 38:L01308, doi:10.1029/2010GL045235
- WILLIAMS SDP, BOCK Y, FANG P, JAMASON P, NIKOLAIDIS RM, PRAWIRODIRDJO L, MILLER M, JOHNSON J (2004) *Error analysis of continuous GPS position time series*. J Geophys Res 109:B03412, doi:10.1029/2003JB002741